

Pixel-In-Pixel Net: Towards Efficient Facial Landmark Detection in the Wild

Haibo Jin, Shengcai Liao, and Ling Shao

Inception Institute of Artificial Intelligence (IIAI), Abu Dhabi, UAE
{haibo.jin, shengcai.liao, ling.shao}@inceptioniai.org

Abstract. Recently, heatmap regression based models become popular because of their superior performance on locating facial landmarks. However, high-resolution feature maps have to be either generated repeatedly or maintained through the network for such models, which is computationally inefficient for practical applications. Moreover, their generalization capabilities across domains are rarely explored. To address these two problems, we propose Pixel-In-Pixel (PIP) Net for facial landmark detection. The proposed model is equipped with a novel detection head based on heatmap regression. Different from conventional heatmap regression, the new detection head conducts score prediction on low-resolution feature maps. To localize landmarks more precisely, it also conduct off-set predictions within each heatmap pixel. By doing this, the inference time is largely reduced without losing accuracy. Besides, we also propose to leverage unlabeled images to improve the generalization capability of our model through image translation based data distillation. Extensive experiments on four benchmarks show that PIP Net is comparable to state-of-the-arts while running at 27.8 FPS on a CPU.

1 Introduction

Facial landmark detection aims to locate predefined landmarks on a human face, the result of which is useful for several face analysis tasks, such as face recognition [25,14,13], face tracking [11], face editing [26], etc. These applications usually run an online system in an uncontrolled environment, which requires a facial landmark detector to be both computationally efficient and robust in unconstrained conditions.

Despite the fact that the performance of facial landmark detectors has been largely advanced by deep learning in recent years [16,30,17,3,5,33,15,32,1,24], developing a computationally efficient facial landmark detection framework still remains a challenge. The current deep learning based methods can be roughly categorized into two types: coordinate regression and heatmap regression. Coordinate regression based methods directly regress the coordinates of facial landmarks through a fully connected layer. Because the result of a fully connected layer is actually a fixed weighted sum of the global feature map, it is usually robust in terms of global shape but inaccurate in details. Therefore, many works

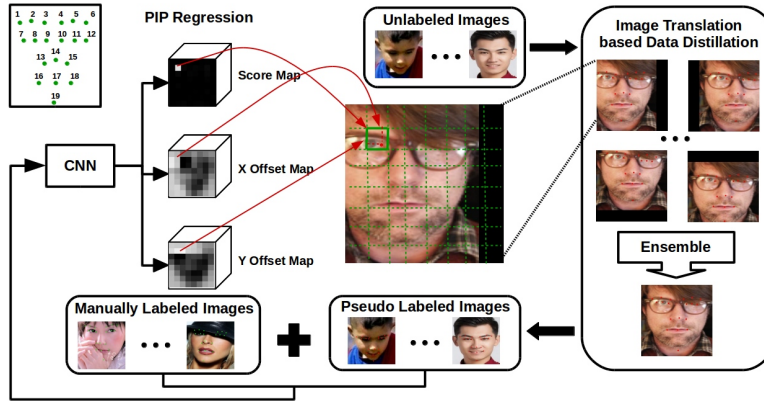


Fig. 1. The overall pipeline of PIP Net. PIP Net locates facial landmarks through PIP regression, which predicts scores and offsets on heatmaps at the same time. The model estimates pseudo-labels for unlabeled images by ensembling multiple translations of the images. After getting pseudo-labels, the manually labeled images and pseudo-labeled images are combined to retrain the detector

cascade coordinate regression in a two-stage [16,5] or multi-stage [28] architecture to get refined predictions, which can lead to slow inference speed. Heatmap regression based methods learn a likelihood heatmap for each landmark and use the location with the highest response as the prediction. Several state-of-the-art methods [24,3,19,35] are based on heatmap regression, which indicates the potential of such a method. However, heatmap regression has to generate high-resolution feature maps through upsampling layers to get precise locations, which takes considerable time during inference. Hence, to get a faster but also accurate facial landmark detector is challenging yet rewarding.

Testing on faces captured in unconstrained conditions is another challenge of this area. Human faces captured in an uncontrolled environment can have large variations in pose, expression, brightness and visibility. Quite a few prior works aim to solve this problem by proposing various new modules [35,32,15,33,17,30]. Different from them, we believe training on large-scale and diverse training data can help alleviate the problem based on the observation that performance gaps exist between different domains of data (see details in Section 4.4). However, it is labour-intensive to get a large number of annotated facial landmark datasets. Therefore, we argue that effective utilization of massive unlabeled images from various domains is promising for obtaining robust facial landmark detectors.

In this paper, we propose a facial landmark detection framework, Pixel-In-Pixel (PIP) Net, to address the two problems above. In order to achieve a faster inference speed, we propose a novel detection head for the task, which is lightweight and accurate at the same time. The proposed detection head, denoted as PIP regression, can be seen as a low-resolution version of heatmap regression.

In other words, PIP regression does not generate high-resolution feature maps through upsampling layers, resulting in an accelerated inference. In addition to score prediction on heatmaps, PIP regression also conducts offset predictions within each heatmap pixel through simple convolutional layers. By doing this, the localization of landmarks becomes more precise with only marginal extra cost. During inference, the heatmap pixel with the highest response and its corresponding offset together determine the location of the predicted landmark. It is worth noting that PIP regression is a single-stage method because the score and offset predictions are independent to each other, and can thus be computed in parallel. Furthermore, we propose a semi-supervised learning method to address the second problem. The proposed method is based on data distillation [20], which attempts to generate a pseudo-label for an unlabeled image by ensembling the results of different image transformations. In contrast to the original data distillation, we use image translation as the transformations rather than scaling and flipping. Such a modification is due to our observation that facial landmark detectors are prone to overfitting to image positions, especially for cross-domain datasets. That is to say, the model can be easily disturbed by background noise at certain positions on a cross-domain image, which can lead to more false positives. To tackle this issue, we intentionally weaken the effect of such noise by ensembling the results of multiple image translations in different directions (i.e., reduce the chance that certain noises appear at certain positions). By doing this, the model can be more robust on estimating pseudo-labels against cross-domain images. Figure 1 gives the overall pipeline of PIP Net. To better evaluate the robustness of the proposed method, we also propose a new training and testing scenario, denoted as Testing on Multiple Domains (TMD). Through extensive experiments, we show that PIP Net gives comparable results to the best existing works on four popular benchmarks, while being lightweight and fast.

Our contributions in this work are summarized as follows: (1) We propose a novel detection head for facial landmark detection, which achieves comparable accuracy to heatmap regression while being much faster; (2) For the first time, we propose to utilize unlabeled images from various domains to address the robustness issue of facial landmark detection through semi-supervised learning; (3) We observe that deep learning based facial landmark detectors easily overfit to specific positions, which can act like a prior on shape constraints but may also result in false positives on cross-domain images. Based on this observation, we propose to use image translation based data distillation for semi-supervised facial landmark detection; (4) We perform extensive experiments on popular facial landmark datasets in different scenarios, which demonstrate the superiority of the proposed PIP Net.

2 Related Work

In this section, we review relevant works on supervised facial landmark detection (coordinate regression models and heatmap regression models), semi-supervised facial landmark detection and the model robustness issue.

Coordinate Regression Models. Coordinate regression directly maps an input image to landmark coordinates. In the context of deep learning, the features of the input image are usually extracted using a Convolutional Neural Network (CNN), and then mapped to coordinates through fully connected layers. Due to its fixed connections to feature maps, the predictions of coordinate regression are inaccurate in details. Therefore, coordinate regression is usually cascaded [5,16] or integrated with extra modules [30,33] to improve its accuracy.

Heatmap Regression Models. Heatmap regression maps an image to high-resolution heatmaps, where each map represents one landmark prediction. During inference, the location with the highest response on each heatmap is used. There are several paradigms for obtaining high-resolution heatmaps. Hourglass [18,15] has been shown to perform well through repeated downsampling and upsampling modules. CPM [29,3] is a sequential architecture composed of CNNs, where the predictions are increasingly refined at each stage. Xiao et al. [31] proposed a simple but effective architecture to obtain high-resolution heatmaps through a few deconvolutional layers. Sun et al. [24] designed a high-resolution network for landmark detection and several other vision tasks by maintaining high-resolution representations through the whole network.

Robustness on Facial Landmark Detection. Feng et al. [5] proposed to use a two-stage framework to mitigate the performance degradation problem. Zhu et al. [33] designed a geometry-aware module to address the occlusion problem. In addition to a global-context module, Merget et al. [17] also applied a PCA-based shape model as a postprocessing step to filter outliers. Dong et al. [3] proposed a style-aggregated approach to handle the large intrinsic variance of image styles. Liu et al. [15] proposed a lightweight global heatmap correction unit to recover outliers after heatmap regression. To obtain a robust facial landmark detector, Zou et al. [35] designed a hierarchical structured landmark ensemble model to automatically discover the most robust patterns on both local and global structures. Unlike earlier works, we propose to use semi-supervised learning to address the robustness problem.

Semi-supervised Facial Landmark Detection. Qian et al. [19] proposed to augment training images through style translation. Honari et al. [8] proposed a module to leverage unlabeled images by maintaining the consistency of predictions with respect to different image transformations. Although we also use image transformations, there is a fundamental difference since we apply image transformations to self-training framework, while Honari et al. [8] used it in an unsupervised manner. Robinson et al. [22] designed an adversarial training framework to leverage unlabeled data. Dong and Yang [4] applied an interaction mechanism between a teacher and students to a self-training framework, where the teacher learns to estimate the quality of the pseudo-labels generated by students. Different from [4], we leverage unlabeled images by improving the accuracy of the predicted pseudo-labels, which is an orthogonal approach to theirs. If necessary, a selection strategy can also be used to filter unqualified pseudo-labels in our framework to further boost the performance.

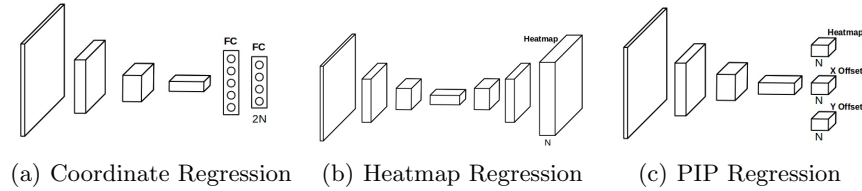


Fig. 2. Comparison of the proposed PIP regression and the existing detection heads in terms of architecture

3 Our Method

In this section, we first introduce PIP regression (Section 3.1), and then present the proposed semi-supervised learning framework (Section 3.2).

3.1 PIP Regression

The existing facial landmark detectors can be categorized into two classes: coordinate regression and heatmap regression, which are defined according to the type of detection head. As we can see from Figure 2(a), coordinate regression outputs a vector with length $2N_{lms}$ through fully connected layers, where N_{lms} represents the number of landmarks. As for heatmap regression (Figure 2(b)), it first gradually upsamples the extracted feature maps to the same (or close) resolution as the input, then outputs a heatmap with N_{lms} channels, where each channel reflects the likelihood of the corresponding landmark location. By comparing the two detection heads, it is easy to see that coordinate regression is more computationally efficient on locating a point, because heatmap regression needs to either upsample the feature maps repeatedly [18,31,15] or maintain high-resolution feature maps through the network [24]. However, heatmap regression has been shown to consistently outperform coordinate regression in terms of detection accuracy [35,24,4]. Despite the inefficiency, heatmap regression is able to achieve state-of-the-art accuracy with a single-stage architecture, while coordinate regression usually needs two or more stages. Accordingly, we would like to ask, is it possible to get a detection head that is efficient and accurate at the same time?

We propose a novel detection head, denoted as PIP regression (Figure 2(c)), which is built upon heatmap regression. We argue that upsampling layers are not necessary for locating points on feature maps. That is to say, low-resolution feature maps are sufficient for localization. By applying heatmap regression on low-resolution feature maps, we obtain coarse estimations of landmarks. To obtain more precise predictions, we also apply offset prediction within each heatmap pixel, where each offset is relative to the top-left corner of the pixel on the x -axis and y -axis. The training loss of PIP Net can be formulated as follows.

$$L = \alpha L_{score} + L_x + L_y, \quad (1)$$

where L_{score} is the loss for the score prediction, L_x and L_y are losses for the offset prediction on the x - and y -axis, respectively, and α is a balancing coefficient. Concretely, L_{score} , L_x and L_y are formulated as

$$L_{score} = \sum_i (S_i^* - S_i')^2, \quad S_i^* \in \{0, 1\} \quad (2)$$

$$L_x = \sum_{S_i^*=1} (X_i^* - X_i')^2, \quad L_y = \sum_{S_i^*=1} (Y_i^* - Y_i')^2, \quad X_i^*, Y_i^* \in [0, 1] \quad (3)$$

where $*$ and $'$ denote ground-truths and estimates. During inference, the final prediction of a landmark is computed as the pixel location with the highest response refined by its offsets on the corresponding channel.

A hyper-parameter of PIP regression is the stride of the network. Given the image size and net stride, the size of a heatmap can be determined as follows.

$$H_{map} = \frac{H_{image}}{S_{stride}}, \quad W_{map} = \frac{W_{image}}{S_{stride}}, \quad (4)$$

where H_{image} and W_{image} are the height and width of the input image, and S_{stride} denotes the net stride. Intuitively, PIP regression can be seen as a general case of the two existing detection heads. When the net stride is equal to the image size (i.e. $H_{map} = W_{map} = 1$), and the score prediction module is cancelled, PIP regression can be seen as coordinate regression, where the conventional fully connected layers are replaced by convolutional layers. When the net stride is equal or close to 1, and the offset prediction is cancelled, then PIP regression is equivalent to heatmap regression. Furthermore, compared to heatmap regression, the optimization of PIP regression during training is easier because low-resolution heatmap is less sensitive to the smoothness of the ground-truth labels. In all the experiments, we simply set the relevant pixel to one and the others to zeros, while heatmap regression requires Gaussian smoothness on ground-truths [31,24].

3.2 Semi-supervised Facial Landmark Detection

The Scenario. As mentioned in Section 1, we propose to use semi-supervised learning to mitigate the robustness issue of facial landmark detectors. Because earlier works do not associate semi-supervised learning with model robustness, their training and testing scenario is impractical. Specifically, a conventional setting for semi-supervised learning is to train and test on a single dataset. Although some works [4,22] utilize unlabeled data from a different domain, their testing set is still restricted to one domain, which does not reflect the realistic situations. To close the gap between the evaluation scenario and practical applications, we propose a new training and testing setting, named Testing on Multiple Domains (TMD). Accordingly, the conventional setting is denoted as Testing on a Single Domain (TSD). The main differences between the two scenarios are two-fold:

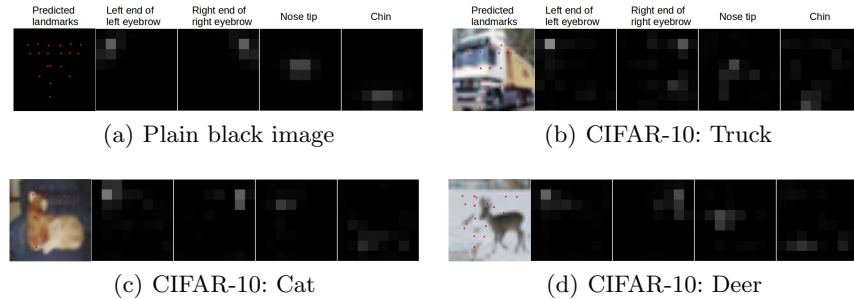


Fig. 3. Landmarks predicted (red dots) on images without human faces. Heatmaps of four landmarks are also presented to show the positions of reponses. (a) Training and testing on plain black images. (b)-(d) Training on face images, and testing on CIFAR-10 images that do not contain human faces

- (1) A model is tested on multiple domains in the TMD scenario, while only one domain is involved in the TSD scenario;
- (2) Not every domain in the TMD scenario has labeled data, while the single testing domain in TSD usually has labeled data from the same domain.

Image Translation based Data Distillation. The proposed semi-supervised learning algorithm is built upon data distillation [20]. Data distillation is an improved self-training method. Different from the conventional self-training [27], data distillation predicts pseudo-labels of unlabeled data by ensembling multiple transformations of the input on a single model. In [20], they applied data distillation to multi-person keypoint detection and general object detection, where image scaling and horizontal flipping were used as the geometric transformations. As for facial landmark detection, we find that horizontal flipping (we do not consider scaling) is not as good as image translation.

As pointed out by [10], a CNN is able to encode position information through zero paddings. In other words, the neurons of a CNN know which part of an image it is looking at. To verify this conclusion, we train a facial landmark detector where the training images are all plain black images but the ground-truth landmarks are unchanged. Then, we input a plain black image for testing, and the predictions are shown in Figure 3(a), Column 1. As we can see from the figure, the model memorizes the most likely positions of the landmarks, which proves its ability of perceiving absolute positions. Therefore, a CNN does learn what (semantic features) and where (absolute position) jointly [10]. Different from multi-person keypoint detection and general object detection, facial landmark detection locates landmarks through a cropped face image, where the facial features are correlated to certain positions (despite the augmentation techniques during training, such as translation and rotation). To validate this, we train a model with normal face images but test on images without human faces. As shown in Column 1 of Figure 3(b)- 3(d), the model still gives landmark predic-

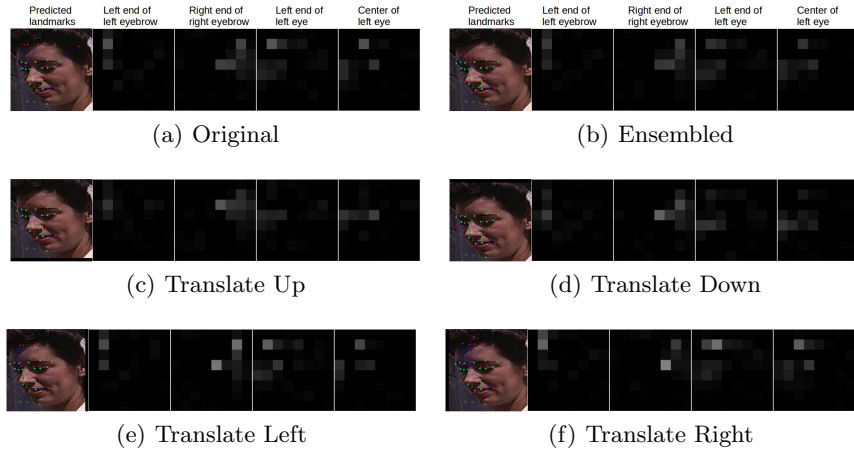


Fig. 4. An example of image translation based data distillation. (a) Predicted landmarks (red dots) as well as ground-truths (green dots) on a cross-domain image. Heatmaps of four landmarks are also visualized for better understanding. (b) The ensemble predictions and heatmaps from four translated images. (c)-(f) Predictions and heatmaps of four translated images (10 pixels up, down, left and right) respectively

tions close to the human face, even if there is no information of facial features. That is to say, position information also contributes to the response of heatmaps. So what does this mean? On one hand, it is a good thing because it acts like a prior that helps restrict the locations of landmark predictions. On the other hand, it can also be seen as overfitting to positions, which may cause false positives when tested on cross-domain data. Figure 4(a), Column 1 shows the predictions of a model trained on COFW while the test image is from WFLW. It is easy to find that several predicted landmarks (red dots) are far from the ground-truths (green dots), which is a bit confusing because the false positives are not really visually similar to the real landmarks. We argue that this is because positions of image patches also matter, in addition to semantic features. More specifically, if some background patch (especially the one from a different domain) happens to be at certain positions, it may generate a higher response than the real landmark. By observing the heatmaps in Figure 4(a), Column 2-5, we can find that the response of the real landmarks are slightly lower than the false positives. To address this problem, we introduce image translation to reduce the chance of noise being at certain positions. As shown in Figure 4(c)- 4(f), with slight translations in different directions (namely 10 pixels up, down, left and right), the predictions can change intensely. Among them, some make the predictions much better (Figure 4(c) and 4(d)) while some make it even worse (Figure 4(f)). Overall, by ensembling the results of the four translations, the false positive problem is significantly alleviated (see Figure 4(b)). Although rotation and horizontal flipping can achieve similar effects as translation, their results are inferior (see Section 4.4).

According to the above observation, we adopt the image translation based data distillation method to semi-supervised facial landmark detection. The pipeline of the algorithm can be simply described in the following steps: (1) Train the facial landmark detector with manually labeled data; (2) Estimate pseudo-labels on multiple translations of the unlabeled data with the trained detector; (3) Ensemble the pseudo-labels of each unlabeled data by averaging the predicted landmark locations; (4) Retrain the detector with the combination of manually labeled data and pseudo-labeled data. Step(2) to (4) are repeated until the model converges. Empirically, we find the model converges after three iterations, which is used in all the experiments. For the translation operation, we conduct two translations (20 and 30 pixels) in each direction (up, down, left, right), so there are eight translations in total for ensembling.

4 Experiments

To demonstrate the effectiveness of the proposed method, we perform experiments on four benchmarks and one dataset captured in a realistic surveillance scenario. We introduce the datasets in Section 4.1 and the experimental settings in Section 4.2. In Section 4.3 and 4.4, we give the experimental results for the supervised learning scenario and semi-supervised learning scenario, respectively. Finally, we compare the inference speed of PIP Net with existing models in Section 4.5.

4.1 Datasets

300W. This dataset [23] provides 68 landmarks for each face, where the face images are collected from LFPW, AFW, HELEN, XM2VTS and IBUG. Following [21], all 3148 training images are from the training set of LFPW and HELEN, and the full set of AFW. The 689 testing images are from the testing set of LFPW and HELEN, and the full set of IBUG. The testing images are further divided into two sets: the common set (554 images) and the challenging set (135 images), where the common set is from LFPW and HELEN, and the challenging set is from IBUG.

COFW. This dataset [2] contains 1345 training images and 507 testing images, where the face images have large variations and occlusions. 29 landmarks are provided for each face.

WFLW. This dataset [30] consists of 7500 training images and 2500 testing images from WIDER Face, where each face has 98 annotated landmarks. The faces in WFLW introduce large variations in pose, expression and occlusion. The testing set is further divided into six subsets for a detailed evaluation, namely, pose (326 images), expression (314 images), illumination (698 images), make-up (206 images), occlusion (736 images) and blur (773 images).

AFLW. This dataset [12] contains 25,000 face images in total, where 20,000 of them are training images, and the remaining 5000 are for testing. Following [34], we use 19 landmarks of AFLW for training and testing.

Table 1. A comparison of PIP Net with different net strides in supervised learning scenario. The image size is 256×256 . The NME (%) results are evaluated on 300W full set, using inter-ocular as normalization

Method	Net Stride	Heatmap Size	Full
PIP Net	16	16×16	3.82
PIP Net	32	8×8	3.52
PIP Net	64	4×4	3.82
PIP Net	128	2×2	4.90

Table 2. A comparison of detection heads in supervised learning scenario. The NME (%) results are evaluated on the 300W full set, using inter-ocular as normalization

Method	Coord Net	Map Net $S_{stride} = 4$	Map Net $S_{stride} = 2$	Map Net $S_{stride} = 1$	PIP Net
Test	5.31	4.52	3.78	3.54	3.52

UCCS. This dataset [7] is originally for face detection and recognition tasks in unconstrained conditions, collected from a university campus through high-resolution surveillance camera. To make it applicable to facial landmark detection, we detect faces with face detectors and manually filter the unqualified ones. We then annotate the cropped 3010 faces from the validation set following the 19 landmarks in AFLW, which will be used as the testing set. The 14,811 faces from the training set remain unlabeled for the semi-supervised learning scenario.

4.2 Experimental Settings

Implementation Details. The face images are cropped according to the provided ground-truths, where the bounding box height and width are S_{scale} times the height and width of the minimum enclosed rectangle of the landmarks ($S_{scale} = 1.3$ for 300W; $S_{scale} = 1.5$ for COFW; $S_{scale} = 1.2$ for WFLW; we use the provided bounding boxes for AFLW). The cropped images are then resized to 256×256 . We use ResNet-18 pretrained on ImageNet as the backbone by default. We also use ResNet-50 in some experiments to explore better results. Adam is used as the optimizer. The total number of training epochs is 60. The initial learning rate is 0.0001, decayed by 10 at epoch 30 and 50. The batch size is 16. We set the balancing coefficient α to 10. The data augmentation includes translation (± 30 pixels on x -axis and y -axis, $p = 0.5$), occlusion (rectangle with maximum 102 pixels as length, $p = 0.5$), horizontal flipping ($p = 0.5$), rotation (± 30 degrees, $p = 0.5$) and blurring (Gaussian blur with maximum 5 radius, $p = 0.3$).

Evaluation Metrics. To compare with most previous works, we use normalized mean errors (NME) to evaluate our models, where the normalization distance is inter-ocular for 300W, COFW and WFLW. As for AFLW and UCCS, we use image width as the normalization distance, following [24].

4.3 Supervised Learning Scenario

Hyper-parameters. Table 1 shows the results of our model with different S_{stride} on the full 300W test set. From the table, $S_{stride} = 32$ gives the best result. Intuitively, it is a trade-off between score prediction and offset prediction. When the net stride is too large, the heatmap size will be small. Thus, the accuracy of the heatmap score prediction will be good, but the offset prediction will be inaccurate because of the large receptive field. Consequently, we use $S_{stride} = 32$ for the remaining experiments.

Baselines. To verify the effectiveness of the proposed detection head, we compare it with the existing ones, namely, coordinate regression and heatmap regression. We implement Coord Net, using ResNet-18 as the backbone. Coord Net consists of three fully connected layers, each of which has 512, 512 and $2N_{lms}$ channels, respectively, where N_{lms} is the number of landmarks. Due to the batch normalization layers inside the head, Coord Net is trained with a batch size of 32 and 120 epochs. Following [31], we implement Map Net with ResNet-18. Specifically, the heatmap regression in [31] is of net stride 4, considering the model speed. During inference, in addition to the location of the highest response, there is also a quarter offset in the direction from the highest response to the second highest response. The rest of the settings are the same as PIP Net. Table 2 gives the results of the three detection heads on the 300W test set. As we can see, PIP Net is the best among the three. Although we claim that PIP regression is faster than heatmap regression, we do not expect PIP regression to be much more accurate. Thus, we suspect that the reduced heatmap resolution makes the accuracy of Map Net drop. We further train Map Net with a net stride of 2 and 1, the results of which are also in Table 2. As expected, the Map Net with net stride 1 (i.e. the heatmap resolution is the same as that of the input image) has a comparable accuracy to PIP regression, but at a large cost on inference speed (see Table 8). It is worth noting that the radius of Gaussian smoothness on ground-truth labels needs to be changed adaptively when the net stride varies so that Map Net can achieve optimal performance. For the Map Net in this work, we use 1, 2 and 4 as the radii for net stride 4, 2 and 1, respectively. On the other hand, the Gaussian radius of PIP Net is set to 1 in all the experiments, which indicates that PIP regression is easier to train than heatmap regression.

Comparison with State-of-the-arts. We compare PIP Net with state-of-the-art methods on four benchmarks. Table 3 shows the results on 300W, COFW and AFLW. From the table, we observe that PIP Net with ResNet-50 achieves new state-of-the-art on COFW and AFLW. PIP Net with ResNet-18 is also quite competitive among the best existing models. When comparing it to similar lightweight models (e.g., ODN), PIP Net with ResNet-18 achieves much better results. Table 4 gives the results on WFLW. As can be seen, our PIP Nets achieve comparable results to the best existing models. Also, it is worth noting that AS w. SAN uses ResNet-152 as the backbone, which is much heavier than ours.

Table 3. A comparison with state-of-the-art methods on 300W, COFW and AFLW for supervised learning. The results are in NME (%), using inter-ocular as the normalization distance

Method	Year	Backbone	300W			COFW	AFLW
			Full	Com.	Cha.	Full	Full
RAR [32]	2016	-	-	-	-	6.03	-
RCN [9]	2016	-	5.41	4.67	8.44	-	5.6
DAC-CSR [6]	2017	-	-	-	-	6.03	-
LAB [30]	2018	Hourglass	3.49	2.98	5.19	5.58	1.85
PDB [5]	2018	ResNet-50	3.60	3.01	6.01	-	1.47
SAN [3]	2018	ResNet-152	3.98	3.34	6.60	-	1.91
RCN+ [8]	2018	-	4.90	4.20	7.78	-	1.61
HG+SA+GHCU [15]	2019	Hourglass	-	-	-	-	1.60
TS ³ [4]	2019	Hourglass+CPM	3.78	3.17	6.41	-	-
LaplaceKL [22]	2019	-	4.01	3.28	7.01	-	1.97
HG-HSLE [35]	2019	Hourglass	3.28	2.85	5.03	-	-
ODN [33]	2019	ResNet-18	4.17	3.56	6.67	5.3	1.63
AS w. SAN [19]	2019	ResNet-152	3.86	3.21	6.49	-	-
HRNet [24]	2019	HRNetV2-W18	3.32	2.87	5.15	3.45	1.57
PIP Net (ours)	-	ResNet-18	3.52	3.09	5.26	3.21	1.51
PIP Net (ours)	-	ResNet-50	3.39	2.96	5.16	3.08	1.47

Table 4. Comparison with state-of-the-art methods for the supervised learning scenario. The NME (%) results are evaluated on the WFLW pose set, expression set, illumination set, make-up set, occlusion set, blur set and full set, using inter-ocular as the normalization

Method	Year	Backbone	Pose	Expr.	Illu.	M.u.	Occ.	Blur	Full
PDB [5]	2018	ResNet-50	8.75	5.36	4.93	5.41	6.37	5.81	5.11
LAB [30]	2018	Hourglass	10.24	5.51	5.23	5.15	6.79	6.32	5.27
HRNet [24]	2019	HRNetV2-W18	7.94	4.85	4.55	4.29	5.44	5.42	4.60
AS w. SAN [19]	2019	ResNet-152	8.42	4.68	4.24	4.37	5.60	4.86	4.39
PIP Net (ours)	-	ResNet-18	8.02	4.77	4.50	4.44	5.66	5.29	4.64
PIP Net (ours)	-	ResNet-50	7.94	4.67	4.48	4.37	5.67	5.27	4.55

Table 5. Comparison with state-of-the-art methods in the TSD scenario. The NME (%) results are evaluated on the 300W full set, using inter-ocular as the normalization

Method	Year	Backbone	10%	20%	50%
RCN+ [8]	2019	-	6.32	5.88	5.45
TS3 [4]	2019	Hourglass+CPM	5.64	5.03	-
PIP Net (ours)	-	ResNet-18	3.95	3.75	3.56

Table 6. NME (%) results of PIP Net in TMD scenario. 300W (300), COFW (C) and their combination is used as labeled training data and the remaining training images are used as unlabeled data. The model is evaluated on all the domains for each setting. The normalization term is image width

Training		Testing				
Labeled	Unlabeled	300W	COFW	WFLW	AFLW	UCCS
300W	×	1.32	2.83	3.18	3.61	7.03
300W	✓	1.29 (+2.3%)	2.64 (+6.7%)	2.62 (+17.6%)	3.08 (+14.7%)	5.62 (+20.0%)
COFW	×	2.64	1.84	4.69	4.42	6.14
COFW	✓	2.43 (+8.0%)	1.76 (+4.3%)	3.95 (+15.8%)	3.76 (+14.9%)	5.57 (+9.3%)
300, C	×	1.34	1.87	3.03	3.44	5.52
300, C	✓	1.31 (+2.2%)	1.87 (+0.0%)	2.56 (+15.5%)	2.93 (+14.8%)	4.70 (+14.9%)

4.4 Semi-supervised Learning Scenario

Testing on a Single Domain. For image translation based data distillation, we first compare our model to state-of-the-art methods in the TSD scenario, though it is not proposed for such a scenario specifically. Table 5 shows the results on 300W, where part of the training data is used with labels and the rest is unlabeled. PIP Net achieves the best results for three settings with different ratios of labeled data, which indicates its promising performance.

Testing on Multiple Domains. As mentioned in Section 3.2, we propose a new scenario, TMD, to conduct a more realistic evaluation for semi-supervised facial landmark detection. We use 300W, COFW, WFLW, AFLW and UCCS to simulate datasets from different domains. In order to evaluate performance across datasets, we unify the annotations of all the datasets to the 19 landmarks of AFLW (see Figure 1, top left corner). Luckily, most landmarks of the datasets are shared and the others can be calculated using the landmarks nearby. Now we have a joint dataset of five subsets with the same landmark definitions. Each subset has a labeled testing set. We choose 300W, COFW and their combination to be the labeled training data, respectively. Aside from the labeled data, the training images of all other datasets is the unlabeled data. The results are tested on the reannotated testing sets of all five datasets, where image width is used as the normalization. Table 6 gives the relevant results. First, we can clearly see the performance gaps when the testing set is from a different domain than the training set. After applying the proposed method, the testing results on all the domains are consistently improved. Particularly, the accuracy on UCCS, a dataset collected from a realistic environment, is significantly improved (10% to 20%) even though there is no labeled data for such a scenario.

Ablation Study. We conduct ablation studies on image translation based data distillation to demonstrate its effectiveness. Since image translation is the key to our method, we also replace it with other image transformations. Table 7

Table 7. Ablation study on translation based data distillation

Scenario	Transformation	Training		300W	Testing	
		Labeled	Unlabeled		300W	UCCS
TSD	None	300W(10%)	300W(90%)	4.05	-	
	Flipping	300W(10%)	300W(90%)	4.00	-	
	Rotation	300W(10%)	300W(90%)	4.00	-	
	Translation	300W(10%)	300W(90%)	3.95	-	
TMD	None	300, C	W+A+U	1.33	4.94	
	Flipping	300, C	W+A+U	1.32	4.92	
	Rotation	300, C	W+A+U	1.34	4.94	
	Translation	300, C	W+A+U	1.31	4.70	

Table 8. A comparison on inference speed in FPS

Model	Year	Backbone	GPU	CPU
LAB [30]	2018	Hourglass	16.7	-
PDB [5]	2018	ResNet-50	30	8
LaplaceKL [22]	2019	-	-	4.9
Map Net (S=4)	-	ResNet-18	102	11.9
Map Net (S=2)	-	ResNet-18	74	3.9
Map Net (S=1)	-	ResNet-18	37.6	1.1
PIP Net (ours)	-	ResNet-50	61	13.6
PIP Net (ours)	-	ResNet-18	114	27.8

shows the comparison of different image transformations in both TSD and TMD scenarios. From the TSD results on 300W, we see that translation is better than flipping and rotation, as well as not using any transformations. For the TMD scenario, translation also out performs the others on the 300W and UCCS testing sets. By comparing flipping and rotation to no transformations, we see that they can improve the performance as well. However, when we combine flipping and rotation with translation, we do not observe obvious improvement.

4.5 Speed

Finally, we do a comparison on inference speed between our model and the existing models. Table 8 gives the Frames Per Second (FPS) results on both a GPU and CPU. PIP Net with ResNet-18 is considerably faster than prior models. Thanks to the lightweight PIP regression, even PIP Net with ResNet-50 has a competitive speed.

5 Conclusions

In this work, we propose a novel facial landmark detection framework named PIP Net. Thanks to the proposed lightweight detection head, the new model achieves competitive results to state-of-the-art methods, while still running in real-time on a CPU. Additionally, PIP Net has been shown to be more robust on testing images from various domains by leveraging unlabeled data through the proposed translation based data distillation method.

Acknowledgements

We would like to thank Yanan Wang, Xuezhi Liang and Jinpeng Li for assistance with UCCS facial landmark annotation. We also appreciate Anna Hennig for comments that greatly improved the manuscript.

References

1. Bulat, A., Tzimiropoulos, G.: How far are we from solving the 2d & 3d face alignment problem? (and a dataset of 230,000 3d facial landmarks). In: ICCV (2017)
2. Burgos-Artizzu, X.P., Perona, P., Dollr, P.: Robust face landmark estimation under occlusion. In: ICCV (2013)
3. Dong, X., Yan, Y., Ouyang, W., Yang, Y.: Style aggregated network for facial landmark detection. In: CVPR (2018)
4. Dong, X., Yang, Y.: Teacher supervises students how to learn from partially labeled images for facial landmark detection. In: ICCV (2019)
5. Feng, Z.H., Kittler, J., Awais, M., Huber, P., Wu, X.J.: Wing loss for robust facial landmark localisation with convolutional neural networks. In: CVPR (2018)
6. Feng, Z.H., Kittler, J., Christmas, W., Huber, P., Wu, X.J.: Dynamic attention-controlled cascaded shape regression exploiting training data augmentation and fuzzy-set sample weighting. In: CVPR (2017)
7. Günther, M., Hu, P., Herrmann, C., Chan, C.H., Jiang, M., Yang, S., Dhamija, A.R., Ramanan, D., Beyerer, J., Kittler, J., Jazaery, M.A., Nouyed, I., Guo, G., Stankiewicz, C., Boulton, T.E.: Unconstrained face detection and open-set face recognition challenge. In: IJCB (2017)
8. Honari, S., Molchanov, P., Tyree, S., Vincent, P., Pal, C., Kautz, J.: Improving landmark localization with semi-supervised learning. In: CVPR (2018)
9. Honari, S., Yosinski, J., Vincent, P., Pal, C.: Recombinator networks: Learning coarse-to-fine feature aggregation. In: CVPR (2016)
10. Islam, M.A., Jia, S., Bruce, N.D.: How much position information do convolutional neural networks encode? In: ICLR (2020)
11. Khan, M.H., McDonagh, J., Tzimiropoulos, G.: Synergy between face alignment and tracking via discriminative globalconsensus optimization. In: ICCV (2017)
12. Koestinger, M., Wohlhart, P., Roth, P.M., Bischof, H.: Annotated facial landmarks in the wild: A large-scale, real-world database for facial landmark localization. In: Proc. First IEEE International Workshop on Benchmarking Facial Image Analysis Technologies (2011)
13. Liao, S., Jain, A.K., Li, S.Z.: Partial face recognition: Alignment-free approach. TPAMI (2013)
14. Liu, W., Wen, Y., Yu, Z., Li, M., Raj, B., Song, L.: Spheroface: Deep hypersphere embedding for face recognition. In: CVPR (2017)
15. Liu, Z., Zhu, X., Hu, G., Guo, H., Tang, M., Lei, Z., Robertson, N.M., Wang, J.: Semantic alignment: Finding semantically consistent ground-truth for facial landmark detection. In: CVPR (2019)
16. Lv, J., Shao, X., Xing, J., Cheng, C., Zhou, X.: A deep regression architecture with two-stage re-initialization for high performance facial landmark detection. In: CVPR (2017)
17. Merget, D., Rock, M., Rigoll, G.: Robust facial landmark detection via a fully-convolutional local-global context network. In: CVPR (2018)

18. Newell, A., Yang, K., Deng, J.: Stacked hourglass networks for human pose estimation. In: ECCV (2016)
19. Qian, S., Sun, K., Wu, W., Qian, C., Jia, J.: Aggregation via separation: Boosting facial landmark detector with semi-supervised style translation. In: ICCV (2019)
20. Radosavovic, I., Dollr, P., Girshick, R., Gkioxari, G., He, K.: Data distillation: Towards omni-supervised learning. In: CVPR (2018)
21. Ren, S., Cao, X., Wei, Y., Sun, J.: Face alignment via regressing local binary features. TIP (2016)
22. Robinson, J.P., Li, Y., Zhang, N., Fu, Y., Tulyakov, S.: Laplace landmark localization. In: ICCV (2019)
23. Sagonas, C., Tzimiropoulos, G., Zafeiriou, S., Pantic, M.: 300 faces in-the-wild challenge: The first facial landmark localization challenge. In: ICCV Workshops (2013)
24. Sun, K., Zhao, Y., Jiang, B., Cheng, T., Xiao, B., Liu, D., Mu, Y., Wang, X., Liu, W., Wang, J.: High-resolution representations for labeling pixels and regions. arXiv: 1904.04514 (2019)
25. Taigman, Y., Yang, M., Ranzato, M., Wolf, L.: Deepface: Closing the gap to human-level performance in face verification. In: CVPR (2014)
26. Thies, J., Zollhofer, M., Stamminger, M., Theobalt, C., Niebner, M.: Face2face: Real-time face capture and reenactment of rgb videos. In: CVPR (2016)
27. Triguero, I., García, S., Herrera, F.: Self-labeled techniques for semi-supervised learning: taxonomy, software and empirical study. Knowledge and Information Systems (2013)
28. Valle, R., Buenaposada, J.M., Valdes, A., Baumela, L.: A deeply-initialized coarse-to-fine ensemble of regression trees for face alignment. In: ECCV (2018)
29. Wei, S.E., Ramakrishna, V., Kanade, T., Sheikh, Y.: Convolutional pose machines. In: CVPR (2016)
30. Wu, W.W., Qian, C., Yang, S., Wang, Q., Cai, Y., Zhou, Q.: Look at boundary: A boundary-aware face alignment algorithm. In: CVPR (2018)
31. Xiao, B., Wu, H., Wei, Y.: Simple baselines for human pose estimation and tracking. In: ECCV (2018)
32. Xiao, S., Feng, J., Xing, J., Lai, H., Yan, S., Kassim, A.: Robust facial landmark detection via recurrent attentive-refinement networks. In: ECCV (2016)
33. Zhu, M., Shi, D., Zheng, M., Sadiq, M.: Robust facial landmark detection via occlusion-adaptive deep networks. In: CVPR (2019)
34. Zhu, S., Li, C., Loy, C.C., Tang, X.: Unconstrained face alignment via cascaded compositional learning. In: CVPR (2016)
35. Zou, X., Zhong, S., Yan, L., Zhao, X., Zhou, J., Wu, Y.: Learning robust facial landmark detection via hierarchical structured ensemble. In: ICCV (2019)